



Cooperative hydrogen production and C–C coupling organic synthesis in one photoredox cycle

Jing Wang^a, Ming-Yu Qi^b, Xuxu Wang^b, Wenyue Su^{b,*}

^a College of Chemistry and Molecular Sciences, Hubei Key Laboratory of Electrochemical Power Sources, Wuhan University, Wuhan 430072, Hubei, China

^b State Key Laboratory of Photocatalysis on Energy and Environment, College of Chemistry, Fuzhou University, Fuzhou, 350116, PR China

ARTICLE INFO

Keywords:
C–C coupling synthesis
H₂ production
Mo-S bond
Dual cocatalysts

ABSTRACT

Coupling hydrogen fuel production with selective oxidative organic synthesis in one cooperative manner offers a promising avenue to enable efficient utilization of photoexcited carriers to achieve sustainable chemistry. Herein, a new Mo₂N/Mn_{0.3}Cd_{0.7}S/CoPi photocatalyst is reported for visible-light-driven hydrogen production paired with selectively oxidative C–C bond formation. Mo₂N acting as electron collectors and reduction sites are adsorbed on the Mn_{0.3}Cd_{0.7}S by interfacial Mo-S bond, while CoPi acting as hole collectors and active sites for oxidation reaction are deposited on Mo₂N/Mn_{0.3}Cd_{0.7}S. Remarkably, the synergistic effect of Mo₂N and CoPi dual cocatalysts results in the adjustable flexibility of switching benzaldehyde (BAD) production to C–C coupling synthesis, thus exhibiting the high selectivity of C–C coupling products. Mechanism studies indicate that the C–C coupling reaction occurs through a free radical mechanism. The present work gives insight for achieving highly efficient C–C coupling synthesis with hydrogen evolution by loading dual cocatalysts.

1. Introduction

Photocatalytic water splitting is considered as one of the promising pathways to convert solar energy for the production of clean and renewable chemical energy [1,2]. Most H₂ production studies have focused on the reduction reaction, but paid less attention to the oxidation half-reaction [3,4]. Coupling oxygen evolution with the hydrogen production is the ideal reaction. However, O₂ formation has rarely been reported because of the need for 4 h⁺ per O₂ molecule and its difficult desorption. [5–8] To solve this issue, sacrificial reagents such as lactic acid (LA) are commonly employed to trap holes to improve the reaction efficiency, which however undesirably wastes the energy of holes, brings along useless oxidation products [9–11]. In this context, to construct a dual-functional photocatalytic reaction system pairing selective oxidative organic synthesis and H₂ production in a cooperative manner would enable sufficient utilization of photogenerated electrons and holes to meet the economic and social sustainability goal.

Biomass from raw materials to intermediates is the most renewable earth-abundant source, which can be used as ideal sacrificial reagents [12]. Exploiting biomass derivatives (such as alcohols, amines, and sugars) to consume holes, while leaving electrons for the proton reduction to H₂, significantly contributes to affordable and renewable

energy production [13]. Benzyl alcohol (BA) is important platform compound that can be derived from various biomass resources. Oxidation of benzyl alcohol (BA) to either carbonyls or C–C coupled products and its derivatives is a route to produce useful value-added chemicals [14–16]. To date, most reports are primarily focused on the oxidation of BA to benzaldehyde (BAD). Recently, the progress of C–C synthesis from BA has been reported [17]. For example, the visible light-driven transformation of benzyl alcohol to C–C coupled products on zero-dimensional (0D) CdS quantum dots has been reported, however featuring a poor selectivity with mixture of hydrobenzoin, deoxybenzoin, and benzil [18]. The co-production of benzyl alcohol to its C–C coupling products (benzoin or deoxybenzoin) and hydrogen (H₂) has been achieved on Zn_xIn₂S_{3+x}, [19] but still suffering from the low selectivity of each C–C coupling products. Notably, the C–C coupled products from BA, such as hydrobenzoin (HB) and benzoin (BZ), can be used as versatile structural motifs in fine chemicals and pharmaceutical intermediates that have a broad range of applications in chiral and synthetic chemistry [20,21].

In this work, we report Mn_{0.3}Cd_{0.7}S nanorods modified with synergistic dual cocatalysts CoPi and Mo₂N bifunctional reaction system enabling efficient visible-light-driven H₂ production and simultaneous transformation of BA to value-added C–C coupled products in one redox

* Corresponding author.

E-mail address: suweny@fzu.edu.cn (W. Su).



cycle. The results demonstrate that the CoPi can be an oxidation active site to accumulate photo-generated holes, while the Mo₂N can capture and transport the photo-generated electrons and provide the active site for H₂ production. Due to such synergistic effect of CoPi and Mo₂N cocatalysts, the photo-induced carriers can be efficiently separated, leading to a higher performance for photocatalytic H₂ production and effectively tunes the product selectivity of BA oxidation. In addition, the in-situ electron paramagnetic resonance (EPR) spectroscopic measurements show that the C_α radical is an important intermediate for BA oxidation, proving that the C–C coupling occurs through a free radical mechanism. It is hoped that this work could open a new horizon for designing novel heterogeneous photocatalysts based cooperative photoredox systems toward simultaneous use of photogenerated electrons and holes pairs for solar-to-chemical energy conversion to value-added fuels and organic chemicals.

2. Experimental section

2.1. Materials

Thioacetamide (CH₃CSNH₂), ethylenediamine (C₂H₄(NH₂)₂), cadmium acetate dehydrate (Cd(CH₃COO)₂·2H₂O), sodium phosphate monobasic ((NaH₂PO₄)₂·2H₂O), manganese acetate tetrahydrate (Mn(CH₃COO)₂·4H₂O), disodium hydrogen phosphate ((Na₂HPO₄)₂·12H₂O), cobalt nitrate (Co(NO₃)₂·6H₂O), molybdenum (> 99% purity), H₂O₂ (> 30%), sodium sulfide nonahydrate (Na₂S·9H₂O), sodium sulfite (Na₂SO₃) and chloroplatinic acid (H₂PtCl₆·6H₂O, 37.5% Pt basis) were obtained from Sinopharm Chemical Reagent Co., Ltd.

2.2. Materials synthesis

2.2.1. Synthesis of Mo₂N nanoparticles (NPs)

Mo₂N NPs was synthesized by calcining MoO₃ in NH₃ atmosphere. In detail, 1 g molybdenum powder was dissolved into 15 mL of H₂O₂ (30%) under constant stirring. After stirring for 45 min, transferred to a Teflon-lined autoclave and maintained at 180 °C for 48 h. The samples were cooled down to ambient temperature, and the precipitate was separated by filtration by washing with DI water. The as-prepared molybdenum trioxide nanowires (MoO₃ NWs) were obtained after freeze-dried. The molybdenum nitride nanoparticles (Mo₂N NPs) were obtained by calcining the MoO₃ samples in NH₃ for 6 h at 750 °C. The XPS result (Fig. S1) shows that passivation layer is formed on the surface of the synthesized sample, and the surface molybdenum is mixed with Mo⁶⁺, Mo⁴⁺ and Mo³⁺, and the stoichiometric ratio of molybdenum to nitrogen in the samples determined by ICP-AES and elemental analysis is about 2:1 (Table S1).

2.2.2. Synthesis of Mn_{0.3}Cd_{0.7}S nanorods (NRs)

The Mn_{0.3}Cd_{0.7}S NRs were prepared by a solvothermal method. Detailed preparation process was demonstrated in supporting information.

2.2.3. Preparation of Mo₂N/Mn_{0.3}Cd_{0.7}S (Mo/MCS) composites

A certain amount of the Mo₂N (2 mg/mL) suspension was added to MCS aqueous suspension (2 mg/mL). The mixture was stirred vigorously for 2 h without light, washed with deionized water and dried at 80 °C to obtain aMo/MCS samples (a = 5, 7 and 10, the mass percentage of Mo₂N to MCS).

2.2.4. Preparation of Mo₂N/Mn_{0.3}Cd_{0.7}S/CoPi (Mo/MCS/Co) composites

Cobalt phosphate cocatalyst was loaded on the Mo/MCS sample by photodeposition method. Typically, 40 mg 7Mo/MCS was dispersed in 50 mL 0.1 M phosphate buffer solution (pH = 7.0), a certain amount of Co(NO₃)₂·6H₂O is added, then the composite is obtained by centrifugation and washing after stirring for 2 h under irradiation, and denoted as 7Mo/MCS/bCo (b = 1, 2 and 3, the mass percentage of CoPi to MCS).

The blank CoPi and MCS/Co composite were prepared by the same procedure without adding 7Mo/MCS and replacing 7Mo/MCS with MCS.

2.3. Characterization

The instrument model used for characterization was demonstrated in the support information, which was reported in our previous works [9]. Detailed experimental process was demonstrated in supporting information.

2.4. Photocatalytic Testing

The photocatalytic hydrogen (H₂) production integrated with hydrobenzoin (HB) synthesis was performed in a double-walled quartz reactor and the temperature of the solution was maintained at 25 °C by a flow of circulating water. Typically, 10 mg samples were added into 10 mL of CH₃CN containing 50 μL (0.48 mmol) of BA. The reaction suspension was purged with Ar gas for 30 min. A 300 W Xe lamp (PLS-SXE 300D, Beijing Perfectlight Co., Ltd.) was used as the light source ($\lambda \geq 420$ nm), and the light power density is 300 mW cm⁻² measured by a photoradiometer (PL-MW2000, Beijing Perfectlight Co., Ltd.). The evolved H₂ was quantified by a gas chromatograph (Shimadzu GC-8A 2014 C). The liquid products were analyzed by high-performance liquid chromatography (HPLC) analysis (Shimadzu HPLC-LC20AT), which also were monitored by gas chromatography–mass spectroscopy (Shimadzu GC–MS QP 2020, Q-Exactive).

2.5. Charge Flow Tracking by Photo-deposition

Photo-deposition of 1.5 wt% Pt and PbO₂ on the surfaces of 7Mo/MCS/2Co was carried out using H₂PtCl₆ and Pb(NO₃)₂ as precursors, respectively, which was reported in our previous works [9].

3. Results and discussion

3.1. Morphology analysis

The overall fabrication procedure for Mo₂N/Mn_{0.3}Cd_{0.7}S/CoPi (Mo/MCS/Co) composite is schematically pictured in Fig. 1a. The scanning electron microscopy (SEM) shows the obtained MoO₃ sample (Figs. S2a and 1b) is a 1D nanowires (NWs) structure, after the NH₃ reduction process, the obtained black sample is Mo₂N nanoparticles (NPs) (Figs. S2b and 1c). Subsequently, the Mo₂N/Mn_{0.3}Cd_{0.7}S (Mo/MCS) composites were prepared by electrostatic self-assembly method. The opposite charged surfaces of Mo₂N and MCS (Fig. S3) result in them assemble into Mo/MCS composites driven by the forces of electrostatic attraction. Finally, the cobalt phosphate (CoPi) have been deposited on the Mo/MCS composites through a photodeposition method. Co²⁺ ions can be oxidized into Co³⁺ by photogenerated holes of MCS NRs and the Co³⁺ has limited solubility at aqueous buffer solution with pH = 7, cobalt phosphate (CoPi) will deposit on the surface of Mo/MCS composites [22]. To check the microscopic morphology and structure information of the dual-cocatalysts composite, transmission electron microscopy (TEM) has been executed. As revealed in Fig. 1e, the 7Mo/MCS/2Co composite shows 1D nanorod morphology, with Mo₂N or CoPi nanoparticles dispersed on its surface. The lattice fringes with a distance of 0.295 nm matches the (211) plane of Mo₂N well. The pronounced lattice spacings of 0.287 and 0.241 nm correspond to the (201) and (110) plane of hexagonal phase MCS, respectively. The lattice fringes with a distance of 0.344 nm matches the (210) plane of CoPi. These results illustrate the successful combination of MCS and Mo₂N/CoPi. In addition, energy-disperse X-ray mapping (EDX-mapping) (Fig. 1f–k) show that the Mo₂N and CoPi nanoparticles dispersed on the surface of MCS.

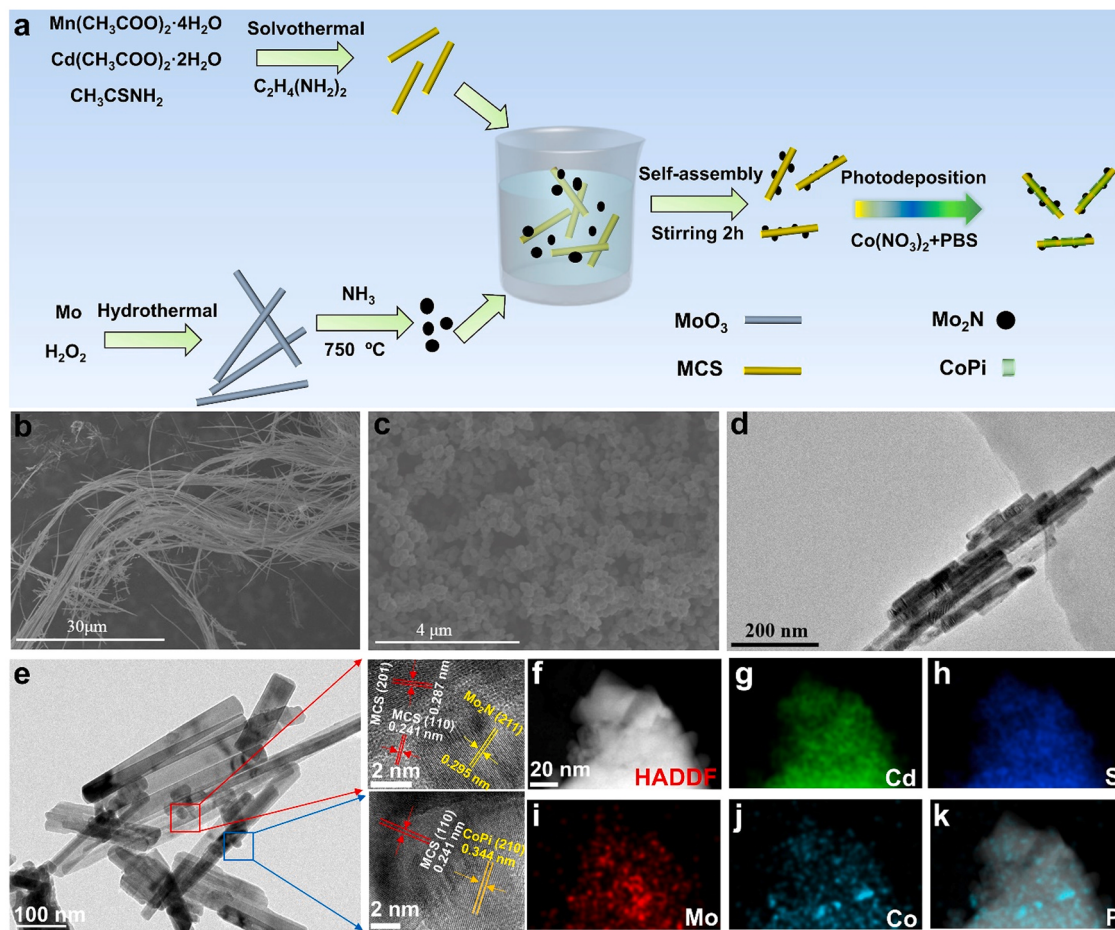


Fig. 1. (a) Schematic diagram for the preparation of Mo/MCS/Co photocatalysts. FESEM images of (b) MoO₃ and (c) Mo₂N. (d) TEM image of MCS, (e) HRTEM image and (f-k) EDX of the 7Mo/MCS/2Co.

3.2. Structural characteristics

The crystal structures of these synthetic samples have been employed by X-ray diffraction (XRD). As shown in Fig. 2a, the diffraction peaks located at 24.9°, 26.6°, 28.5°, 44.2° and 52.5° correspond to (100), (002), (101), (110) and (112) crystallographic planes of hexagonal solid solution Mn_{0.3}Cd_{0.7}S [9]. The diffraction peaks of CoPi are in a good agreement with those of monoclinic Co₃(PO₄)₂·8H₂O (JCPDS NO. 33-0432) [23]. The diffraction peaks located at 37.1°, 42.9°, 62.4° and 74.9° are assigned to (111), (200), (220) and (311) crystallographic planes of cubic Mo₂N (JCPDF 25-1366), respectively. After loading of Mo₂N or/and CoPi on Mn_{0.3}Cd_{0.7}S, the XRD patterns have no obvious changes for 7Mo/MCS, MCS/2Co and 7Mo/MCS/2Co. No diffraction peaks of Mo₂N and CoPi are observed in these composites, and this phenomenon could be ascribed to the lower Mo₂N and CoPi content.

Fig. 2b shows the UV-Vis diffuse reflectance spectroscopy (DRS) of the as-obtained samples. The absorption band edge of CoPi sample locates at around 280 nm, and the optical absorption in the range of 400–700 nm corresponds to the d-d electron transition of Co (II) [24]. The bare Mo₂N presents a broad and intense absorption in the range of 250–800 nm, which is consistent with its black color [25]. The band gap of blank MCS is determined to be of 2.44 eV based on its UV-vis DRS with the Tauc plot (Fig. S4). Compared with the blank MCS NRs, a red shift of optical absorption was observed over all the 7Mo/MCS, MCS/2Co and 7Mo/MCS/2Co composites. N₂ adsorption-desorption tests are conducted to gain information about surface properties of the sample. As listed in Table S2, it can be seen that compared with MCS NRs, the BET specific surface area of 7Mo/MCS, MCS/2Co and

7Mo/MCS/2Co increase from 22.99 m² g⁻¹ to 34.84, 33.17, and 35.02 m² g⁻¹, respectively. The increased surface area may offer abundant exposed catalytic-active sites and improve the photocatalytic activity.

X-ray photoelectron spectrum (XPS) provides valuable chemical composition and binding states of elements on the surface of 7Mo/MCS/2Co composite. As compared with bare MCS NRs, the peaks in both Cd 3d region (411.2 and 404.4 eV) and Mn 2p region (651.8 and 640.8 eV) shifted towards higher binding energy (Fig. 2c, d). As shown in Fig. 2f, the peak at 226.7 eV verified the formation of Mo-S bond, and the existence of Mo-S bonds facilitates the transfer of photo-generated charges [26]. Compared with Mo₂N, the binding energy of Mo 3d and N 1 s of 7Mo/MCS/2Co are negatively shifted, suggesting the existence of interaction among Mo₂N and MCS in the composites (Fig. 2f, g) [27]. In the case of Co 2p XPS spectrum (Fig. 2h), the peaks of Co 2p_{3/2} and Co 2p_{1/2} are located at 781.87 eV, 797.99 eV, 785.52 eV and 801.97 eV (satellite peaks at 788.38 eV and 805.08 eV), which proves the composition of Co²⁺ and Co³⁺ [28]. The P 2p peak at 133.1 eV (Fig. 2i) is indicative of PO₄³⁻ in the CoPi phase [22].

3.3. Photocatalytic performance

The dehydrogenative C–C coupling of benzyl alcohol (BA) into hydrobenzoin (HB) and H₂ performance was evaluated over the as-prepared samples under visible light. It was found that the production rates of H₂ and HB are calculated to be ca. 1.0, suggesting a stoichiometric dehydrogenation reaction. Only relatively low activity for converting BA to benzaldehyde (BAD) appears on MCS (Fig. 3a). Notably,

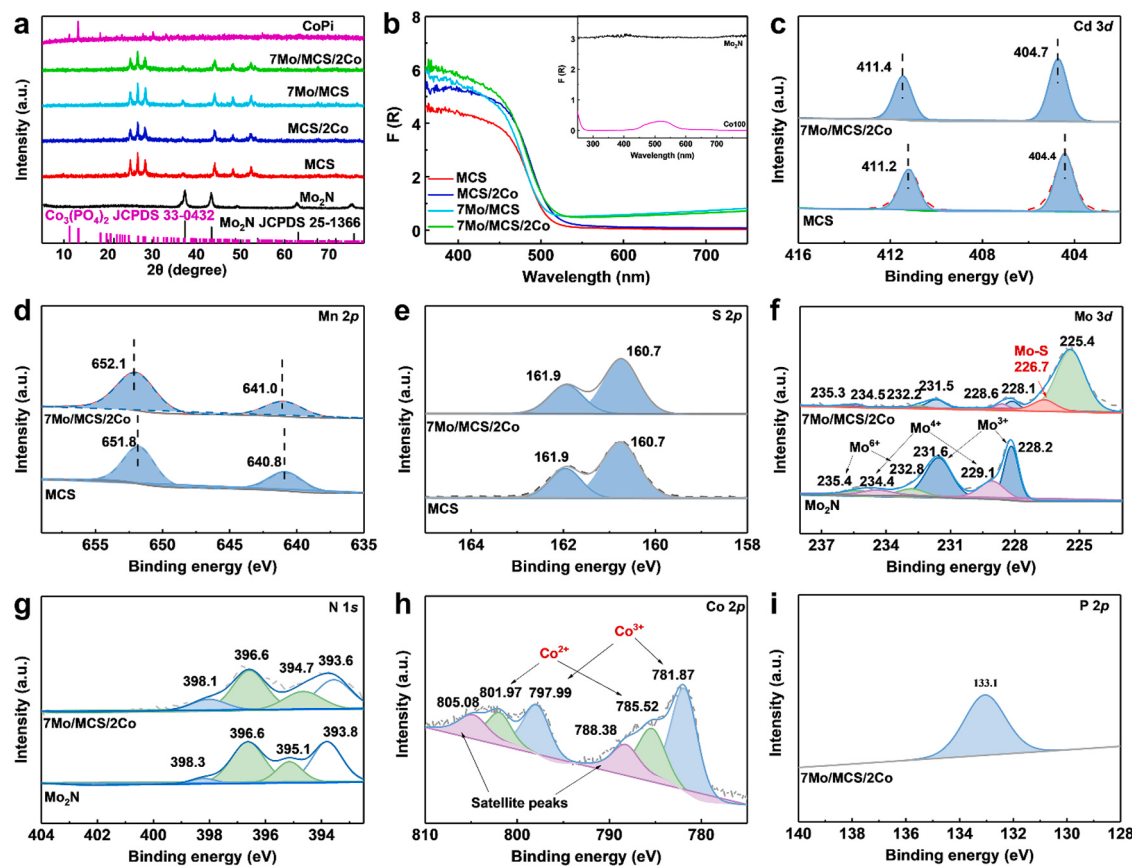


Fig. 2. XRD patterns (a) and UV-vis DRS (b) of Mo₂N, CoPi, MCS, 7Mo/MCS, MCS/2Co and 7Mo/MCS/2Co samples. The high resolution XPS spectra of (c) Cd 3d, (d) Mn 2p, (e) S 2p, (f) Mo 3d, (g) N 1 s, (h) Co 2p, (i) P 2p of the samples.

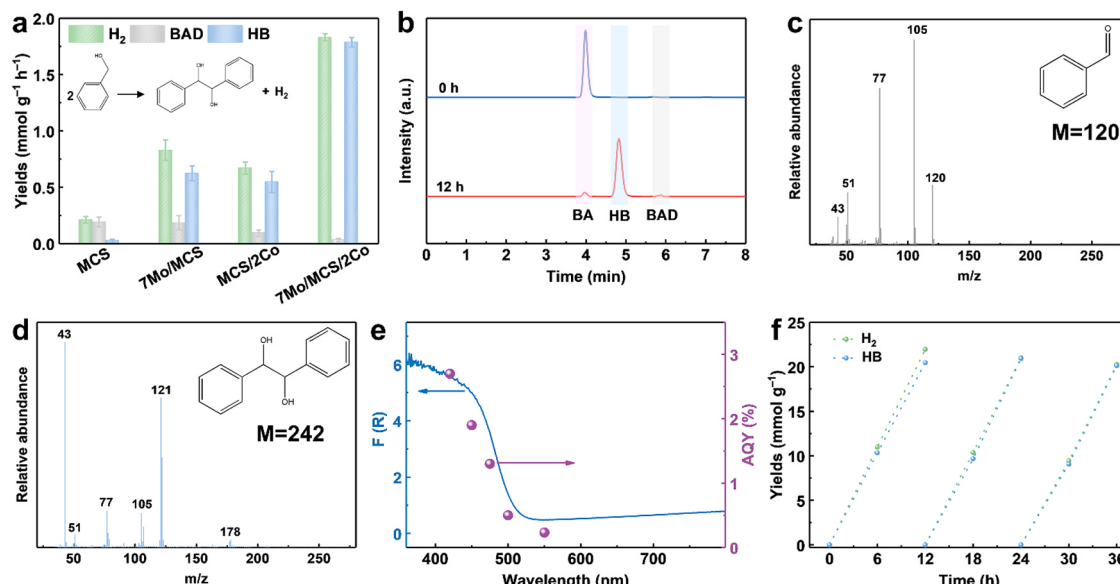


Fig. 3. (a) Activity of photocatalytic H₂ production pairing with HB synthesis of the as-prepared samples, (b) High performance liquid chromatography (HPLC) analysis chromatogram of benzyl alcohol (BA), benzaldehyde (BAD) and hydrobenzoin (HB), Mass spectra of the obtain liquid-products of (c) BAD and (d) HB. (e) DRS spectrum of 7Mo/MCS/2Co composite (left axis) and AQY of HB from C–C coupling of BA versus the incident light wavelength (right axis), (f) Recycling experiments of the 7Mo/MCS/2Co samples.

the introduction of Mo₂N and CoPi onto MCS can not only improve the H₂-generation rate, but also tune the selectivity for BA oxidation (Fig. S6). The as-prepared 7Mo/MCS/2Co shows an optimum performance among the investigated samples (Fig. 3a). The average H₂-

generation rate of 1.83 mmol g⁻¹ h⁻¹ was obtained after 12 h irradiation, which is around 8.71, 2.20 and 2.73 times than that of blank MCS, single cocatalyst loading MCS/2Co and 7Mo/MCS, respectively. Meanwhile, the conversion of BA improves from 6.05% to 35.78%, 29.68%

and 90.20%. Specifically, over 7Mo/MCS/2Co, a HB production rate of $1.79 \text{ mmol g}^{-1} \text{ h}^{-1}$ can be obtained with a yield of 89.45% (12 h reaction time) and a high selectivity of above 98.24% (Fig. 3b-d). The wavelength-dependent HB produced from C–C coupling and AQE measurement of 7Mo/MCS/2Co composite have been performed. The apparent quantum yield (AQY) for the 7Mo/MCS/2Co composite, calculated as the number of charge carriers (holes) used for the HB production divided by the number of incident photons, depends strongly on the light wavelength and well matches the DRS spectrum for the 7Mo/MCS/2Co composite, as shown in Fig. 3e. The corresponding AQE at 420 nm reached 2.71%, which is significantly higher than that of the MCS NRs, 7Mo/MCS and MCS/2Co composite. Moreover, as shown in Supplementary Table S4, it can be found that the photocatalytic activity and selectivity of 7Mo/MCS/2Co composite in BA conversion has exceeded that of most recently reported catalysts. The efficacy of the 7Mo/MCS/2Co composite was also tested for recyclability of three successive runs. No obvious loss of the activity is observed after 3 cycles over a total reaction time of 36 h (Fig. 3f), suggesting its high stability during photocatalytic H₂ evolution and C–C coupling organic synthesis process. The used 7Mo/MCS/2Co sample was further examined by XRD and XPS, and the unchanged XRD pattern and XPS spectrum of the composite are observed (Fig. S7). The results indicate that the 7Mo/MCS/2Co photocatalyst possesses good structural stability in the photocatalytic system.

3.4. Discussion of the photocatalytic mechanism

Photocurrent responses and electrochemical impedance spectra (EIS) were carried out over MCS, 7Mo/MCS, MCS/2Co and 7Mo/MCS/2Co. As shown in Fig. 4a, MCS NRs show the lowest photocurrent density,

while the introduction of Mo₂N or CoPi obviously raises the current density. In particular, when CoPi and Mo₂N are loaded onto MCS NRs simultaneously, the 7Mo/MCS/2Co composite shows the highest photocurrent density. The EIS of 7Mo/MCS/2Co shows the smallest semicircles among the four investigated samples (Fig. 4b), suggesting a most effective electron-hole pairs separation and transport over 7Mo/MCS/2Co. PL spectra and time-resolved photoluminescence spectra (TRPL) have also been performed. As shown in Fig. 4c, the PL emission intensity decreases in the following order: 7Mo/MCS/2Co < MCS/2Co < 7Mo/MCS < bare MCS. And the TRPL spectra (Fig. 4d and Table S3) show that 7Mo/MCS/2Co has the longest charge carrier lifetime among the four samples, indicating that charge recombination can be better suppressed after loading Mo₂N and CoPi.

To reveal the reaction mechanism of HB formation in the photo-redox catalytic system, we conducted a series of control experiments, as disclosed in Fig. 4e. Removing the catalyst or light irradiation, no product was detected, indicating that the reaction is a photocatalytic process. The introduction of a hole scavenger (TEOA) into the system retarded the HB and BAD formation, whereas the formation of H₂ ceased after the addition of an electron scavenger (NaIO₃), showing that both photogenerated electrons and holes participate in the formation of H₂, BAD and HB on the 7Mo/MCS/2Co photocatalyst. In addition, BAD is always kept at a very low concentration during the reaction (Fig. S8), the production rate of HB matches the production rate of H₂ very well, indicating the BAD is not an intermediate product but a by-product [16]. Furthermore, it is noted that the addition of the radical scavenger 5, 5-dimethyl-1-pyrroline-N-oxide (DMPO) also significantly inhibited the production of HB (Fig. 4e), indicating that the formation of HB is through radicals intermediates [29].

To gain more hints on radical intermediates mechanism, the electron

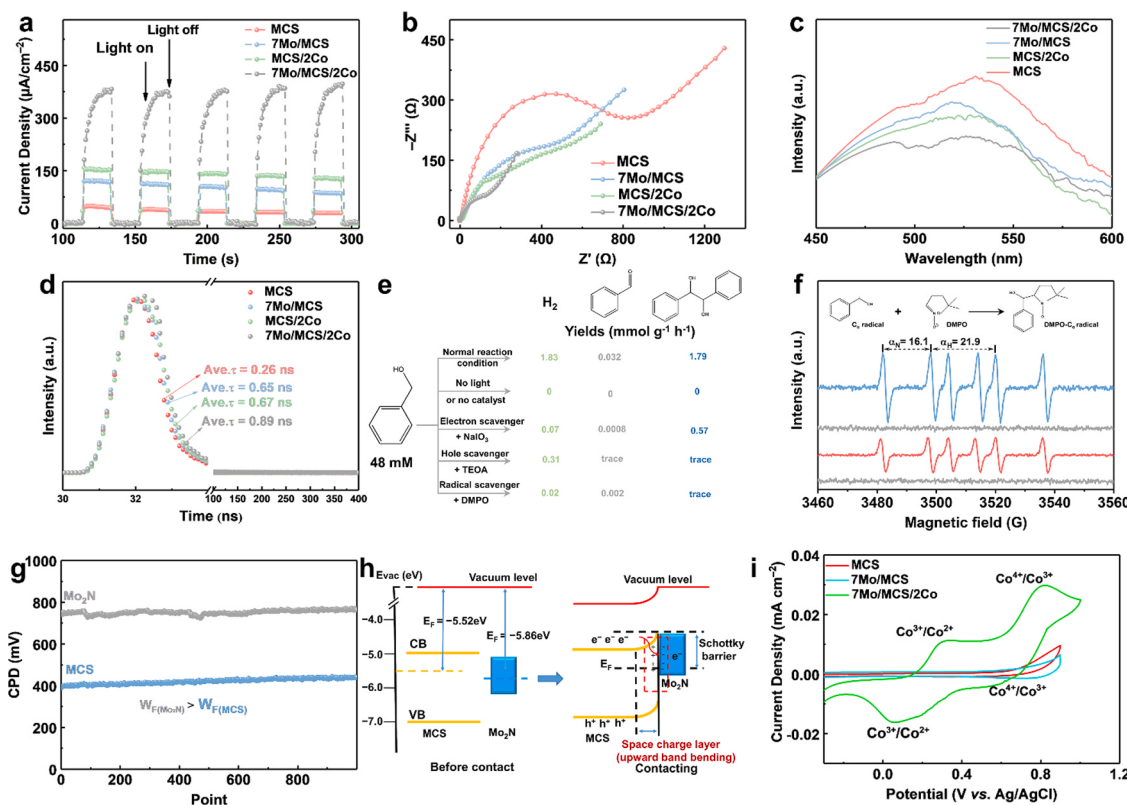


Fig. 4. (a) Transient photocurrent responses, (b) Nyquist impedance plots, (c) Steady-state photoluminescence spectra, (d) Time-resolved photoluminescence spectra decay of MCS, 7Mo/MCS, MCS/2Co and 7Mo/MCS/2Co. (e) Control experiments with different additives catalyzed by 7Mo/MCS/2Co composites. Scavenger concentrations: 24 mM NaIO₃, 24 mM triethanolamine (TEOA), and 24 mM DMPO. Reaction time: 12 h. (f) In situ EPR spectra of MCS and 7Mo/MCS/2Co composites in argon (Ar)-saturated CH₃CN solution in the presence of DMPO. (g) Contact potential difference (CPD) of the MCS and Mo₂N, (h) The Schottky contact between Mo₂N and MCS. (i) Cyclic voltammetry (CV) curves of samples.

paramagnetic resonance (EPR) technique using DMPO as a spin-trapping reagent is utilized to detect the carbon-centered free radicals in this reaction. Fig. 4f shows six characteristic signal peaks belonging to the DMPO-C_α radical adduct under light irradiation for both MCS and the 7Mo/MCS/2Co composite, indicating the existence of carbon-centered radical intermediate in this photocatalytic system. [30] Furthermore, a quantitative analysis has been performed to measure the hydrogen and nitrogen hyperfine plittings (α_H , α_N) for the nitroxide nitrogen. The result suggests $\alpha_H = 21.9$ and $\alpha_N = 16.1$, which are similar to the reported values for DMPO-CH(OH)Ph in the previous literature [14]. In addition, the signal intensities of DMPO-CH(OH)Ph radicals over the 7Mo/MCS/2Co composites are stronger than that for MCS, indicating that a larger amount of such •CH(OH)Ph radicals can be photogenerated in a 7Mo/MCS/2Co-catalyzed system, which is consistent with the photoactivity trend. Consequently, the 7Mo/MCS/2Co photocatalyst markedly favors the C–C coupling of as-obtained •CH(OH)Ph radicals.

The work function (WF) of MCS and Mo₂N were measured by Kelvin probe. As demonstrated in Fig. 4g, the average contact potential difference (CPD) of Mo₂N and MCS are 760 and 420 mV, respectively. Accordingly, the WF of Mo₂N and MCS are calculated to be 5.86 and 5.52 eV, respectively, which indicates that the Fermi level of Mo₂N is

more negative than that of MCS (Fig. 4h). The formation of the Schottky junction at the interface of MCS and Mo₂N makes the electrons transfer from MCS to Mo₂N until equilibrium is reached. And a built-in electric field, with positively charged MCS and negatively charged Mo₂N, is thus formed.

The value of standard potentials of E(Co³⁺/Co²⁺) and E(O₂/H₂O) are + 1.74 and + 1.23 V (vs NHE), respectively, indicating that it is thermodynamically favorable for the photogenerated holes to oxidize Co²⁺ of CoPi to Co³⁺, and Co³⁺ then oxidizes water to oxygen and returns to Co²⁺ [31,32]. It was further supported by the cyclic voltammetry (CV). The CV of 7Mo/MCS/2Co shows two pairs of reversible redox peaks (Fig. 4i), which are assigned to the redox couple of Co^{3+/2+} and Co^{4+/3+}, respectively [33,34]. In contrast, no redox peaks are observed for MCS and 7Mo/MCS.

To verify the photogenerated charge transfer route, the photodeposition of 7Mo/MCS/2Co with Pt or PbO₂ probe was carried out. As shown in Fig. 5a, b, Pt particles are clearly deposited on Mo₂N, while no Pt are observed on MCS or CoPi (Fig. S10), implying that the photogenerated electrons in the 7Mo/MCS/2Co sample transfer from MCS to Mo₂N [9]. As shown in Fig. 5c, d, PbO₂ particles deposited on CoPi, while there are no lattice fringes of PbO₂ on MCS or Mo₂N (Fig. S11),

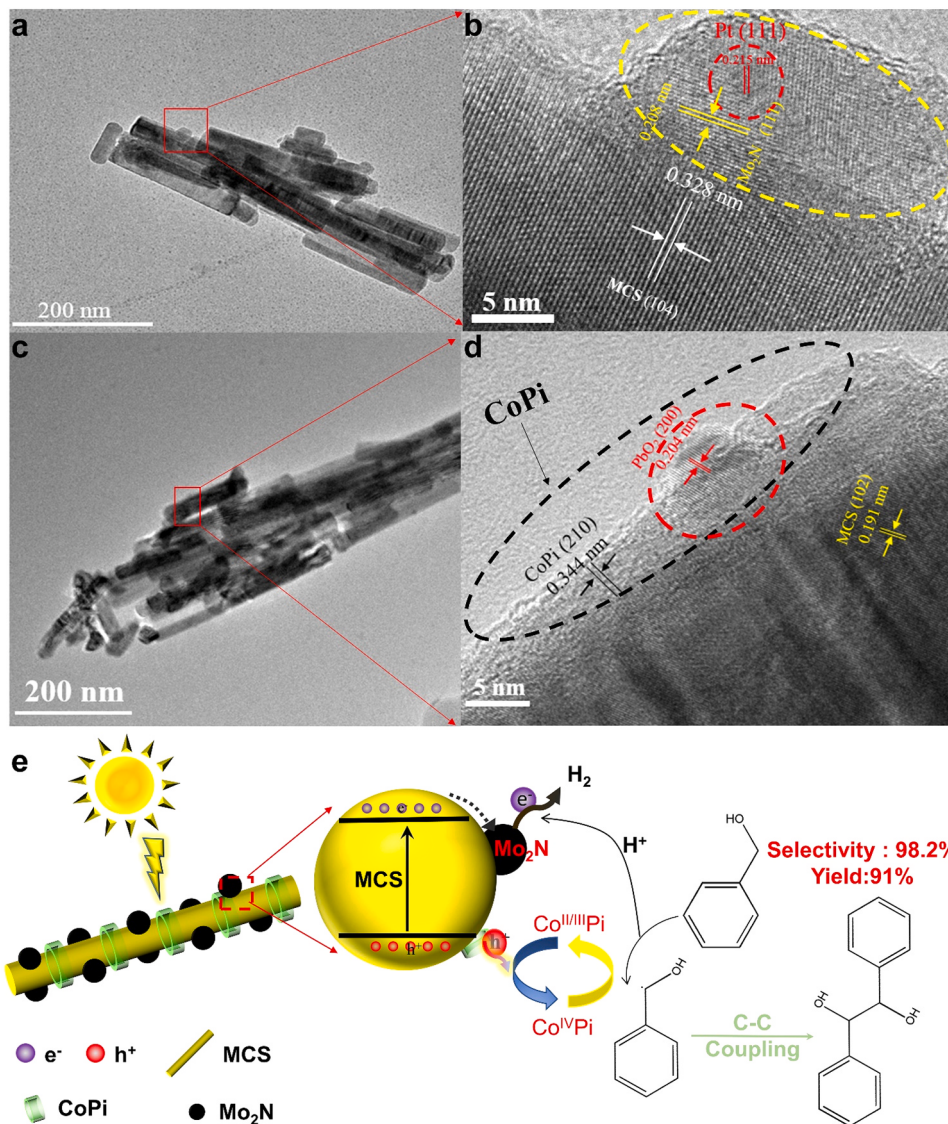


Fig. 5. (a, b) TEM images of 7Mo/MCS/2Co photodeposited with Pt, (c, d) TEM images of 7Mo/MCS/2Co photodeposited with PbO₂. (e) Possible mechanism for the photocatalytic hydrogen evolution of the Mo/MCS/Co samples.

implying that the photogenerated holes of MCS NRs transfer to CoPi [35]. These results convincingly verify that Mo₂N mainly serves as active sites of reduction while CoPi serves as the oxidation sites.

Based on the results presented above, a mechanism for photocatalytic hydrogen production by water splitting over the Mo/MCS/Co composites is proposed in Fig. 5e. Under irradiation, the photoexcited electrons on the VB of MCS NRs are excited to the CB, then transferred to Mo₂N through a interfacial Mo-S bond, and the protons denoted by BA are reduced to H₂. In the meantime, the photoexcited holes on the VB of MCS NRs migrate to CoPi and the Co^{2+/3+} of CoPi is oxidized to Co⁴⁺. Then Co⁴⁺ first oxidize the C–H bond of BA, affording •CH(OH)Ph radicals and returns to Co^{2+/3+}, which promotes the separation of photogenerated holes through the cycle of Co^{2+/3+}→Co⁴⁺→Co^{2+/3+}. Then, the •CH(OH)Ph radicals can either be further oxidized by holes to generate BAD or combine with another •CH(OH)Ph radical to form HB. Therefore, there is a mutual promotion between the CoPi-mediated hole transfer and the Mo₂N-mediated electron transfer, greatly improving the charge separation efficiency, leading to an enhanced photoactivity and selectivity of C–C coupling products compared with MCS.

4. Conclusions

In conclusion, a Mo₂N/Mn_{0.3}Cd_{0.7}S/CoPi composite with spatial separation of oxidation and reduction sites was fabricated by electrostatic self-assembly and photodeposition method. The Mo₂N/Mn_{0.3}Cd_{0.7}S/CoPi composite exhibits remarkably enhanced photocatalytic activities and selectivity of C–C coupling products than that Mn_{0.3}Cd_{0.7}S loaded with single cocatalyst. The excellent photocatalytic activity of Mo₂N/Mn_{0.3}Cd_{0.7}S/CoPi composite can be attributed to the synergistic effect of the Mo₂N and CoPi dual cocatalysts. In particular, the cage-like hole cocatalyst CoPi can be used as the C_α radical intermediates recognition active site to control the adsorption-desorption behavior of the substrate molecule and enhance its interaction with the photocatalyst, thereby exhibiting a superior selectivity of C–C coupling products. The interfacial Mo-S bond formed between Mo₂N and MCS creates direct electron transfer channels and further improves the photocatalytic activity. This work provides a promising route to engineer efficient synergistic dual cocatalysts modified photocatalysts for visible-light-driven cooperative photoredox-catalyzed production of solar fuels and selective organic synthesis of value-added chemical feedstocks. Moreover, to advance the practical applications of such a dual-functional photocatalytic system, besides the rational design and synthesis of highly efficient photocatalysts, it is also an important direction to rationally design continuous flow photoreactor, which can not only increase the interfacial interaction between catalysts and organic substrates induced by the enhanced mass-transfer abilities, but also separate the reactants and target products in time.

CRediT authorship contribution statement

Jing Wang: Conceptualization, Methodology, Resources, Investigation, Writing – original draft. **Mingyu Qi:** Formal analysis. **Xuxu Wang:** Funding acquisition. **Wenyue Su:** Supervision, Writing – review & editing.

Declaration of Competing Interest

The authors declare that they have no known competing financial interests or personal relationships that could have appeared to influence the work reported in this paper.

Acknowledgements

This work is financially supported by the Natural Science Foundation of Fujian Province (2019J01630, 2021L3003), the National Natural Science Foundation of China (Grants No. 21373050, 22172031). The

authors would like to thank Zhang San from Shiyanjia lab (www.shiyanjia.com) for TEM analysis.

Appendix A. Supporting information

Supplementary data associated with this article can be found in the online version at doi:[10.1016/j.apcatb.2021.120812](https://doi.org/10.1016/j.apcatb.2021.120812).

References

- [1] W. Che, W. Cheng, T. Yao, F. Tang, W. Liu, H. Su, Y. Huang, Q. Liu, J. Liu, F. Hu, Z. Pan, Z. Sun, S. Wei, Fast photoelectron transfer in (Cring)-C₃N₄ plane heterostructural nanosheets for overall water splitting, *J. Am. Chem. Soc.* 139 (2017) 3021–3026.
- [2] Z. Xiong, L. Huang, J. Peng, Y. Hou, Z. Ding, S. Wang, Spinel-type mixed metal sulfide NiCo₂S₄ for efficient photocatalytic reduction of CO₂ with visible light, *ChemCatChem* 11 (2019) 5513–5518.
- [3] M.Y. Qi, Y.H. Li, F. Zhang, Z.R. Tang, Y. Xiong, Y.-J. Xu, Switching light for site-directed spatial loading of cocatalysts onto heterojunction photocatalysts with boosted redox catalysis, *ACS Catal.* 10 (2020) 3194–3202.
- [4] M.Y. Qi, M. Conte, M. Anpo, Z.R. Tang, Y.J. Xu, Cooperative coupling of oxidative organic synthesis and hydrogen production over semiconductor-based photocatalysts, *Chem. Rev.* (2021), <https://doi.org/10.1021/acs.chemrev.1c00197>.
- [5] N. Zhang, M.Y. Qi, L. Yuan, X. Fu, Z.R. Tang, J. Gong, Y.J. Xu, Broadband light harvesting and unidirectional electron flow for efficient electron accumulation for hydrogen generation, *Angew. Chem. Int. Ed.* 58 (2019) 10003–10007.
- [6] S. Xu, M.H. Huang, T. Li, Z.Q. Wei, X. Lin, X.C. Dai, S. Hou, X.Y. Fu, F.X. Xiao, Modulating charge migration in photoredox organic transformation via exquisite interface engineering, *J. Mater. Chem. A* 8 (2020) 8360–8375.
- [7] S. Xu, H.J. Lin, X. Lin, X.Y. Fu, S. Hou, Z.Q. Wei, Q.L. Mo, F.X. Xiao, Intercalating ultrathin polymer interim layer for charge transfer cascade towards solar-powered selective organic transformation, *J. Catal.* 399 (2021) 150–161.
- [8] Z.Q. Wei, S. Hou, X. Lin, S. Xu, X.C. Dai, Y.H. Li, J.Y. Li, F.X. Xiao, Y.J. Xu, Unexpected boosted solar water oxidation by nonconjugated polymer-mediated tandem charge transfer, *J. Am. Chem. Soc.* 142 (2020) 21899–21912.
- [9] J. Wang, Y. Zhang, X. Wang, W. Su, Simultaneous enhancements in photoactivity and anti-potocorrosion of Z-scheme Mn_{0.25}Cd_{0.75}S/WO₃ for solar water splitting, *Appl. Catal. B: Environ.* 268 (2020), 118444.
- [10] S. Wang, B.Y. Guan, X. Wang, X.W.D. Lou, Formation of hierarchical Co₉S₈@ZnIn₂S₄ heterostructured cages as an efficient photocatalyst for hydrogen evolution, *J. Am. Chem. Soc.* 140 (2018) 15145–15148.
- [11] H.K. Wu, Y.-H. Li, M.Y. Qi, Q. Lin, Y.J. Xu, Enhanced photocatalytic CO₂ reduction with suppressing H₂ evolution via Pt cocatalyst and surface SiO₂ coating, *Appl. Catal. B: Environ.* 278 (2020), 119267.
- [12] Y. Qin, M. Hao, C. Xu, Z. Li, Visible light initiated oxidative coupling of alcohols and o-phenylenediamines to synthesize benzimidazoles over MIL-101(Fe) promoted by plasmonic Au, *Green. Chem.* 23 (2021) 4161–4169.
- [13] Q. Lin, Y.H. Li, M.Y. Qi, J.Y. Li, Z.R. Tang, M. Anpo, Y.M.A. Yamada, Y.J. Xu, Photoredox dual reaction for selective alcohol oxidation and hydrogen evolution over nickel surface-modified ZnIn₂S₄, *Appl. Catal. B: Environ.* 271 (2020), 118946.
- [14] M.Y. Qi, Y.H. Li, M. Anpo, Z.R. Tang, Y.J. Xu, Efficient photoredox-mediated C–C coupling organic synthesis and hydrogen production over engineered semiconductor quantum dots, *ACS Catal.* 10 (2020) 14327–14335.
- [15] L. Yuan, M.Y. Qi, Z.R. Tang, Y.J. Xu, Coupling strategy for CO₂ valorization integrated with organic synthesis by heterogeneous photocatalysis, *Angew. Chem. Int. Ed.* 60 (2021) 2–25.
- [16] Q. Guo, F. Liang, X.B. Li, Y.J. Gao, M.Y. Huang, Y. Wang, S.G. Xia, X.Y. Gao, Q. C. Gan, Z.S. Lin, C.H. Tung, L.Z. Wu, Efficient and selective CO₂ reduction integrated with organic synthesis by solar energy, *Chem.* 5 (2019) 2605–2616.
- [17] L. Yuan, Y.H. Li, Z.R. Tang, J. Gong, Y.J. Xu, Defect-promoted visible light-driven C–C coupling reactions pairing with CO₂ reduction, *J. Catal.* 390 (2020) 244–250.
- [18] K.P. McClelland, E.A. Weiss, Selective photocatalytic oxidation of benzyl alcohol to benzaldehyde or C–C coupled products by visible-light-absorbing quantum dots, *ACS Appl. Energy Mater.* 2 (2018) 92–96.
- [19] N. Luo, T. Hou, S. Liu, B. Zeng, J. Lu, J. Zhang, H. Li, F. Wang, Photocatalytic coproduction of deoxybenzoin and H₂ through tandem redox reactions, *ACS Catal.* 10 (2019) 762–769.
- [20] X. Sun, D. Jiang, L. Zhang, W. Wang, Alkaline modified g-C₃N₄ photocatalyst for high selective oxide coupling of benzyl alcohol to benzoin, *Appl. Catal. B: Environ.* 220 (2018) 553–560.
- [21] C. Jiang, H. Wang, Y. Wang, H. Ji, All solid-state Z-scheme CeO₂/ZnIn₂S₄ hybrid for the photocatalytic selective oxidation of aromatic alcohols coupled with hydrogen evolution, *Appl. Catal. B: Environ.* 277 (2020), 119235.
- [22] K.Q. Lu, M.Y. Qi, Z.R. Tang, Y.J. Xu, Earth-abundant MoS₂ and cobalt phosphate dual cocatalysts on 1D CdS nanowires for boosting photocatalytic hydrogen production, *Langmuir* 35 (2019) 11056–11065.
- [23] T. Di, B. Zhu, J. Zhang, B. Cheng, J. Yu, Enhanced photocatalytic H₂ production on CdS nanorod using cobalt-phosphate as oxidation cocatalyst, *Appl. Surf. Sci.* 389 (2016) 775–782.
- [24] L. Ge, C. Han, X. Xiao, L. Guo, In situ synthesis of cobalt–phosphate (Co–Pi) modified g-C₃N₄ photocatalysts with enhanced photocatalytic activities, *Appl. Catal. B: Environ.* 142–143 (2013) 414–422.

[25] J. Xie, S. Li, X. Zhang, J. Zhang, R. Wang, H. Zhang, B. Pan, Y. Xie, Atomically-thin molybdenum nitride nanosheets with exposed active surface sites for efficient hydrogen evolution, *Chem. Sci.* 5 (2014) 4615–4620.

[26] X. Wang, X. Wang, J. Huang, S. Li, A. Meng, Z. Li, Interfacial chemical bond and internal electric field modulated Z-scheme $S_v\text{-ZnIn}_2\text{S}_4\text{/MoSe}_2$ photocatalyst for efficient hydrogen evolution, *Nat. Commun.* 12 (2021) 4112.

[27] S. Gong, Z. Jiang, P. Shi, J. Fan, Q. Xu, Y. Min, Noble-metal-free heterostructure for efficient hydrogen evolution in visible region: Molybdenum nitride/ultrathin graphitic carbon nitride, *Appl. Catal. B: Environ.* 238 (2018) 318–327.

[28] M. Barroso, A.J. Cowan, S.R. Pendlebury, M. Gratzel, D.R. Klug, J.R. Durrant, The role of cobalt phosphate in enhancing the photocatalytic activity of alpha- Fe_2O_3 toward water oxidation, *J. Am. Chem. Soc.* 133 (2011) 14868–14871.

[29] S. Xie, Z. Shen, J. Deng, P. Guo, Q. Zhang, H. Zhang, C. Ma, Z. Jiang, J. Cheng, D. Deng, Y. Wang, Visible light-driven C–H activation and C–C coupling of methanol into ethylene glycol, *Nat. Commun.* 9 (2018) 1181.

[30] X. Wu, S. Xie, C. Liu, C. Zhou, J. Lin, J. Kang, Q. Zhang, Z. Wang, Y. Wang, Ligand-controlled photocatalysis of CdS quantum dots for lignin valorization under visible light, *ACS Catal.* 9 (2019) 8443–8451.

[31] B. Pan, Y. Zhou, W. Su, X. Wang, Enhanced photocatalytic CO_2 conversion over LaPO_4 by introduction of CoCl_2 as a hole mediator, *RSC Adv.* 6 (2016) 34744–34747.

[32] G.H. Moon, M. Yu, C.K. Chan, H. Tuysuz, Highly active cobalt-based electrocatalysts with facile incorporation of dopants for the oxygen evolution reaction, *Angew. Chem. Int. Ed.* 58 (2019) 3491–3495.

[33] Y. Sasaki, H. Kato, A. Kudo, [Co(bpy)₃]^(3+/2+) and [Co(phen)₃]^(3+/2+) electron mediators for overall water splitting under sunlight irradiation using Z-scheme photocatalyst system, *J. Am. Chem. Soc.* 135 (2013) 5441–5449.

[34] C. Lee, K. Shin, C. Jung, P.P. Choi, G. Henkelman, H.M. Lee, Atomically embedded Ag via electrodiffusion boosts oxygen evolution of CoOOH nanosheet arrays, *ACS Catal.* (2019) 562–569.

[35] W. Jiang, X. Zong, L. An, S. Hua, X. Miao, S. Luan, Y. Wen, F.F. Tao, Z. Sun, Consciously constructing heterojunction or direct Z-scheme photocatalysts by regulating electron flow direction, *ACS Catal.* 8 (2018) 2209–2217.